

Breaking the vitrification limitation of monatomic metals

Received: 14 June 2023

Accepted: 9 July 2024

Published online: 30 July 2024

 Check for updates

Xing Tong ^{1,7}, Yue-E Zhang ^{1,2,7}, Bao-Shuang Shang ¹, Hua-Ping Zhang ¹, Zezhou Li ³, Yao Zhang ³, Gang Wang ⁴, Yan-Hui Liu ^{1,5}, Yong Zhao¹, Bo Zhang¹, Hai-Bo Ke ¹✉, Jihan Zhou ³✉, Hai-Yang Bai ^{1,5,6}✉ & Wei-Hua Wang ^{1,5,6}

The question of whether all materials can solidify into the glassy form proposed by Turnbull half a century ago remains unsolved. Some of the simplest systems of monatomic metals have not been vitrified, especially the close-packed face-centred cubic metals. Here we report the vitrification of gold, which is notoriously difficult to be vitrified, and several similar close-packed face-centred cubic and hexagonal metals using a method of picosecond pulsed laser ablation in a liquid medium. The vitrification occurs through the rapid cooling during laser ablation and the inhibition of nucleation by the liquid medium. Using this method, a large number of atomic configurations, including glassy configurations, can be generated simultaneously, from which a stable glass state can be sampled. Simulations demonstrate that the favourable stability of monatomic metals stems from the strong topological frustration of icosahedra-like clusters. Our work breaks the limitation of the glass-forming ability of matter, indicating that vitrification is an intrinsic property of matter and providing a strategy for the preparation and design of metallic glasses from an atomic configuration perspective.

In 1948, Kauzmann noticed that all supercooled liquids, if they do not crystallize as they cool, must solidify into a glassy form to avoid the entropy crisis¹, which means that all liquids may be vitrified, and that glass formation is an intrinsic property of a matter. Following this idea, in the 1950s, Turnbull and Cohen successfully supercooled some pure metals^{2,3}, overturning the consensus at the time that pure metals could not be supercooled. Their work led to the birth of new members of the metallic glass (MG) family. Turnbull and Cohen also argued that even pure metals could be vitrified and be stable internally^{3–5}. Over the past decades, huge efforts have been made to vitrify monatomic metals, although the true laboratory demonstration of most of monatomic metallic glasses (MMGs) has not yet been achieved^{6–8}. Only a few

specific monatomic metals, such as the body-centred cubic (bcc) type, have so far been vitrified into MMGs through several specific methods and techniques^{7,9–13}. For example, tantalum (Ta) was vitrified at a high liquid-quenching rate (10^{14} K s⁻¹) by cooling the melted nanotips of the crystalline bridge in a transmission electron microscope⁷. However, even such a high cooling rate cannot vitrify face-centred cubic (fcc) or hexagonal close-packed (hcp) monatomic metals⁷. The failure to vitrify fcc/hcp metals is probably caused by the heterogeneous nucleation and fast crystal growth of the supercooled liquids from the surrounding crystalline metals⁸, which means that heterogeneous nucleation should be avoided for vitrifying close-packed metals. Among the fcc metals, only nickel (Ni) appears to be vitrified into amorphous nanoparticles (NPs)

¹Songshan Lake Materials Laboratory, Dongguan, China. ²College of Physics, Liaoning University, Shenyang, China. ³Beijing National Laboratory for Molecular Sciences, College of Chemistry and Molecular Engineering, Peking University, Beijing, China. ⁴Laboratory for Microstructures, Institute of Materials, Shanghai University, Shanghai, China. ⁵Institute of Physics, Chinese Academy of Sciences, Beijing, China. ⁶Center of Materials Science and Optoelectronics Engineering, University of Chinese Academy of Sciences, Beijing, China. ⁷These authors contributed equally: Xing Tong, Yue-E Zhang.

✉e-mail: kehaibo@sslslab.org.cn; jhzhou@pku.edu.cn; hybai@iphy.ac.cn

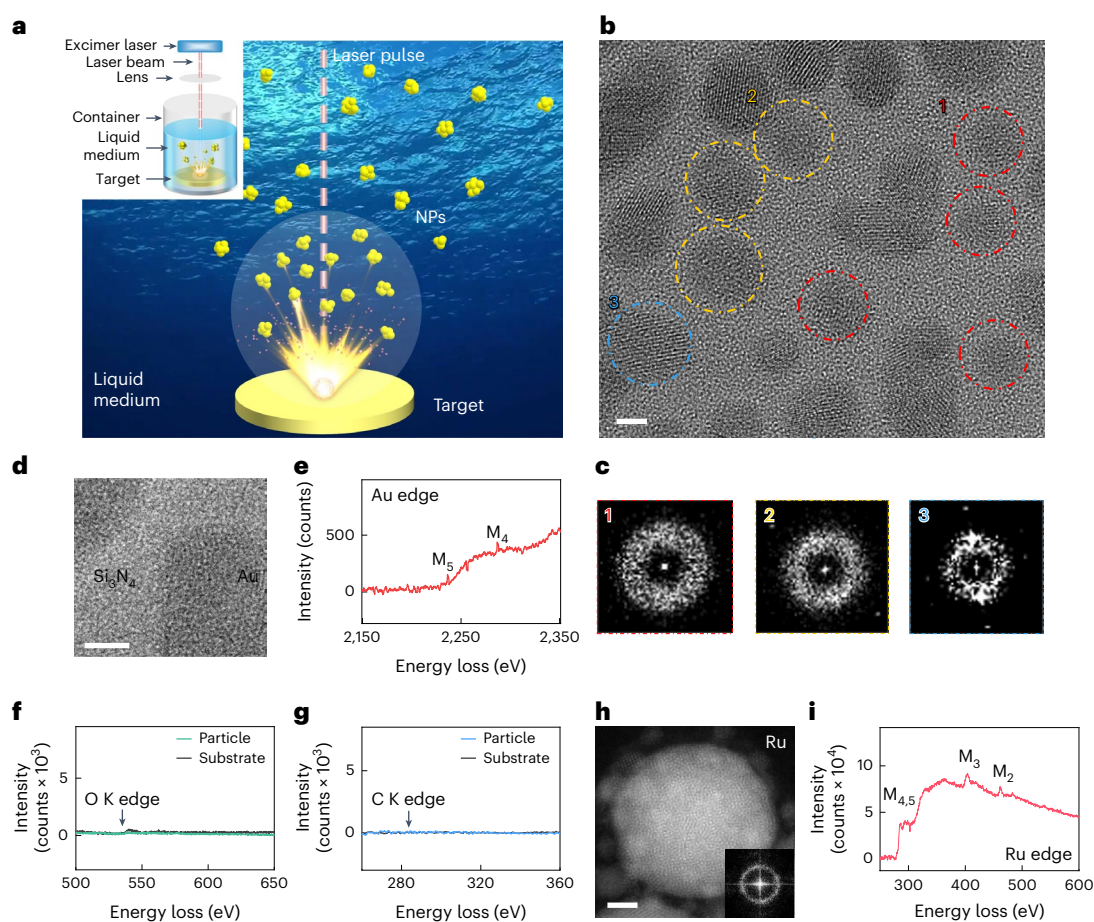


Fig. 1 Illustration of a laser-aided ultrafast quenching approach in ethanol medium and the preparation of fcc (Au) and hcp (Ru) MMGNPs. **a**, Schematic of the MMG formation process via laser ablation in liquid medium. The inset shows the experimental set-up for pulsed laser ablation of the metallic target in a liquid medium. A picosecond pulsed laser is introduced to melt the bulk metal target to form small liquid metal clusters. The metal clusters are simultaneously immersed in the liquid medium and quenched at an ultrafast cooling rate. With such a high cooling rate and amorphous environment (contamination-free liquid), the vitrified MMG NPs can be obtained from all of the chosen metals, that is, Au and Ru. The single yellow sphere in **a** represents a cluster. **b**, HR-TEM image of Au NPs randomly orientated on the substrate, which contains fully amorphous (highlighted by red dot-dashed circles), partially amorphous (yellow dot-dashed circles) and crystalline (blue dot-dashed circles) NPs. Scale bar, 2 nm. **c**, Corresponding FFT of each NP type marked in **b**. **d–g**, TEM image of an Au NP (**d**) and Au (**e**), O (**f**) and C (**g**) EELS spectra of the Au NP, showing that the obtained NP is monatomic. M₄ and M₅ in **e** are the Au edges. In **f**, the O signal on the Si₃N₄ membrane region is higher than that in the Au MMG region, which indicates that the minimal amount of O in the raw spectrum is due to the slightly oxidized Si₃N₄ membrane substrate. After subtracting the background O signal from the substrate, the O signal for the MMG region flattens out. In **g**, no C signal was detected in the EELS spectrum. Scale bar (**d**), 2 nm. **h, i**, Ru high-angle annular dark-field scanning transmission electron microscopy image (**h**) and EELS spectrum of Ru and O (**i**), showing that the Ru NP is amorphous and monatomic. Inset in **h** is the corresponding FFT image. In **i**, a quite weak O signal was detected in the EELS spectrum. M₂–M₅ in **i** are the Ru edges. Scale bar (**h**), 2 nm.

via an atomization method; for other fcc metals, such as gold (Au), this method proved unsuccessful¹¹. Containerless processing^{14,15} and fluxing treatments^{16–19} are used widely to prevent or suppress the heterogeneous nucleation caused by contaminants such as crystals and oxides²⁰ during the glass-forming process. An MG based on palladium (Pd) with a breakthrough size of 80 nm was obtained using a B₂O₃ melt flux in the induction melting process to create a container-free/pollution-free environment¹⁷. Therefore, appropriate media should be considered, combined with melting and rapid quenching processes, to inhibit heterogeneous nucleation and vitrify monatomic close-packed metals.

Glass is known to have many metastable configurations that are located in the widely distributed metabasins of the potential energy landscape (PEL)²¹. When a configuration is in a locally deep sub-basin, topological frustration will beat the ordering process. The amorphous structure can be stabilized with high kinetic stability and even survive at room temperature. However, with traditional methods such as suction casting, the quenching process is always monotonous and can produce only very few configurations in a monolithic glass²², and it is

difficult to obtain the desired stable configurations. Although monatomic metals such as fcc metals have been deposited in the amorphous state at extremely low temperatures (77 K), the resultant amorphous structure cannot survive at room temperature^{8,23}. The amorphous structures are formed in highly unrelaxed and high-energy states, and the stable configurations cannot be obtained, making them inherently less stable⁸. There are no essential differences observed in the overall microstructural statistics or configuration types for the amorphous solids formed through rapid quenching and deposition—both exhibit short-range-ordered but long-range-disordered packings. However, owing to different formation mechanisms, variations in the atomic configuration probabilities exist between these two kinds of amorphous solid, leading to differences in energy, stability, density, free volume and some other properties. Therefore, a method that can produce various configurations, including stable ones, is in urgent need, from which the most stable configuration can be sampled.

Recently, multi-element NPs, including amorphous structures^{24,25}, have been prepared using ultrafast pulsed laser ablation^{25,26}, but no

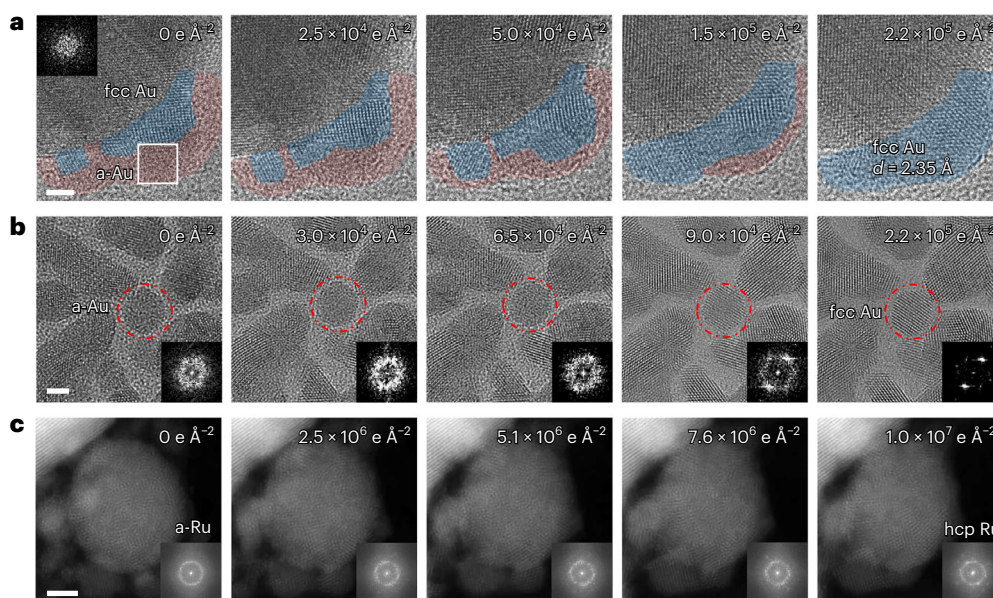


Fig. 2 | The devitrification process of MMGs. a, The electron-induced atomic ordering of Au MMG. The inset contains the FFT image of the area highlighted by the white square and shows the diffuse halo. The areas coloured in red and blue represent the amorphous and crystalline regions, respectively. The evolution of the Au MMG devitrification process was recorded at 25 frames per s. The clear coalescence of crystalline and amorphous Au indicates that the Au is pure. *d* is the lattice spacing. Scale bar, 2 nm. **b, c**, Individual Au MMG (**b**) and Ru

MMG (**c**) NPs were exposed to a high electron dose to capture the respective devitrification processes. The red dot-dashed circle in **b** indicates amorphous Au. The high-resolution TEM (Au) and scanning TEM (Ru) images of the NPs and the corresponding (inset) FFT images of the different steps show the respective disorder-to-order transitions. The electron voltage was 300 kV for the in situ electron irradiation. Scale bars, 2 nm. For each frame in **a–c**, the electron dose is shown in the top corner.

monatomic MG has yet been obtained using this potent method. In our work we present a picosecond pulsed laser ablation method for vitrification of monatomic fcc and hcp metals in a liquid medium at room temperature. A rapid cooling can be achieved during the process of ultrafast pulsed laser ablation in liquid²⁵, where a suitable liquid medium is vital for the suppression of nucleation. More importantly, this method can produce glassy NPs with numerous different configurations in one batch. As a result, the obtained MMGs show various levels of stability, and some of them can retain the amorphous state at room temperature. Molecular dynamics (MD) simulations show that the high stability of the stable MMGs originates from the strong topological frustration of forming icosahedra-like clusters. The diversity of configurations can provide rich candidates of various monatomic metals by which to study many fundamental problems, such as vitrification and devitrification mechanisms shielded by the chemical complexity in multi-element MGs.

Our metal vitrification strategy is illustrated in Fig. 1a (also see Methods). A picosecond pulsed laser was used to ablate bulk metallic targets with ethanol as the solvent and containerless cooling medium (Fig. 1a and Supplementary Table 1). The highest temperature during ablation could reach 10,000 K (ref. 27), at which most monatomic metals can be melted and vaporized to form NPs. The cooling rate in the absorbing media has been reported to be from 10^{10} to 10^{13} K s⁻¹ (ref. 26). Although monatomic Au has been regarded as one of the most difficult metals to vitrify⁴, using our method we successfully obtained MMG NPs from an Au target with an impurity level of less than 0.001% (Supplementary Table 1). We found that many NPs have disordered structures, although some have lattice fringes. Figure 1b and Supplementary Fig. 1a, c show high-resolution transmission electron microscopy (HR-TEM) images of several fully amorphous (red circles), partially amorphous (yellow circles) and crystalline (blue circles) Au NPs. The structures were further confirmed via fast Fourier transforms (FFTs) of the images, which showed a typical diffusive amorphous halo structure, a partially amorphous halo structure with bright spots and a structure with bright spots, marked in red, yellow

and blue, respectively (Fig. 1c and Supplementary Fig. 1b, d). Owing to spatio-temporal fluctuations during the process of pulsed laser ablation in liquid, not all monatomic metallic NPs could be quenched under the ideal conditions for the formation of glass. Thus, a crystalline lattice was also observed. We counted the proportions of the Au NPs with different degrees of amorphization. There is a larger frequency of Au NPs with fully and partially amorphous structures, with a median size of about 4.5 nm (Supplementary Fig. 1e). Electron energy-loss spectroscopy (EELS) was carried out to examine any possible contamination by carbon (C) and oxygen (O) due to the extremely high spatial resolution and analytical sensitivity, especially for light elements (Supplementary Notes). By integrating the spectra in the particle and substrate regions of the EELS maps separately, despite detecting minor O signals from the slight oxidation of the Si₃N₄ substrate, no C or O signal can be observed in the MMG particle regions (Fig. 1d–g), indicating that impurities are below the EELS detection limit (less than 1,000 ppm). Consequently, the formation of the Au MMG is not caused by C or O doping. In addition, the chemical state of Au was examined using X-ray photoelectron spectroscopy (XPS), which indicating only the presence of Au⁰ (Supplementary Fig. 1f). The XPS measurement procedures were carried out by drying and pressing the NPs into the XPS sample holder (Supplementary Notes). All of the results show that the vitrified Au is pure. Besides Au, ruthenium (Ru) MMG NPs were also successfully synthesized (Fig. 1h), which is another type of metal (hcp) that is considered to be difficult to vitrify⁸. The EELS spectrum of the Ru MMG NPs shows that the particles are composed of monatomic Ru without notable amounts of O or C present (Fig. 1i).

The regions of amorphous structure were then irradiated with an electron beam during TEM (Methods). Figure 2a and Supplementary Video 1 show the disorder-to-order transition of the amorphous regions in the Au MMG during electron irradiation. The crystallites grow epitaxially along the boundary, so that the amorphous region is exhausted and coalesces with the crystalline region. Most of the amorphous Au (a-Au) regions (marked in red) transformed into fcc Au crystallites (marked in blue) due to the irradiation at a high voltage

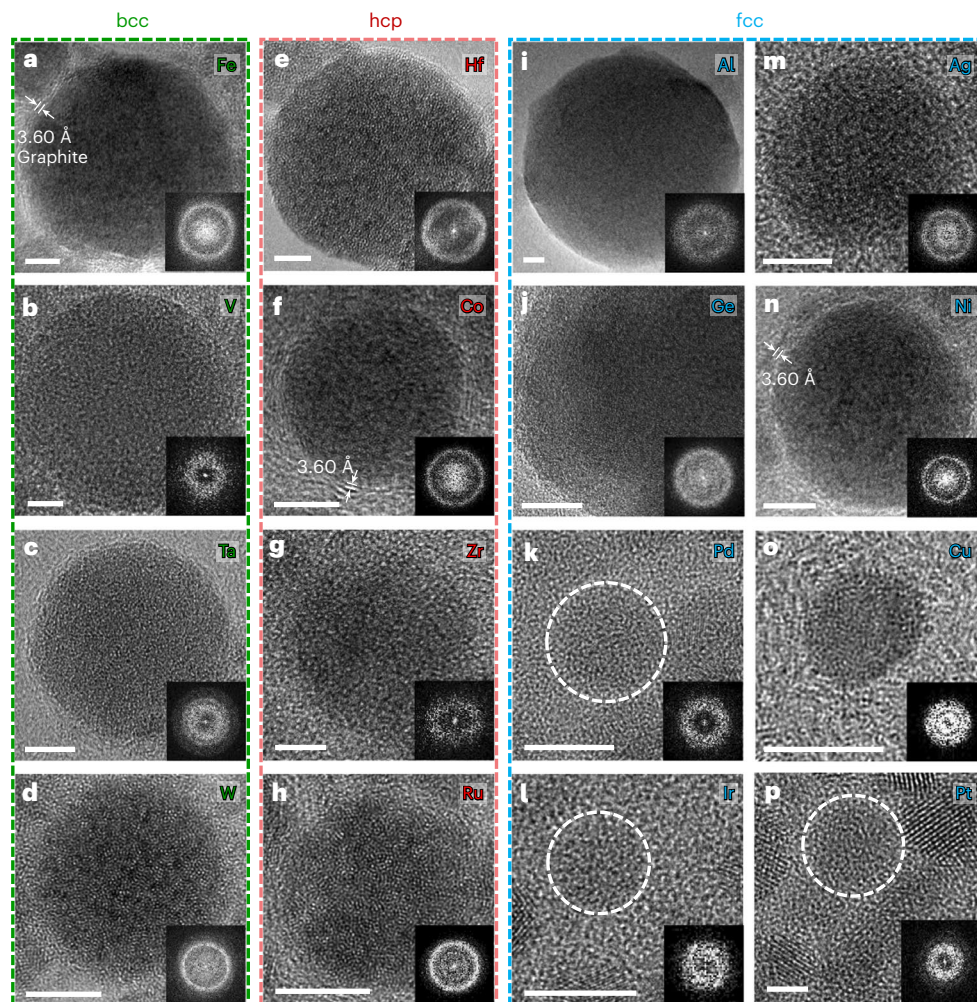


Fig. 3 | Extensive preparation of MMG NPs from monatomic metals that include bcc, hcp and fcc metals. **a–p**, MMG NPs prepared for Fe (**a**), V (**b**), Ta (**c**), W (**d**), Hf (**e**), Co (**f**), Zr (**g**), Ru (**h**), Al (**i**), Ge (**j**), Pd (**k**), Ir (**l**), Ag (**m**), Ni (**n**), Cu (**o**) and Pt (**p**). The bcc, hcp and fcc types of metal are marked in green, red and blue, respectively. The white dashed circles in **k**, **l** and **p** indicate amorphous metals. The insets show the corresponding FFT image of each MMG, showing the diffuse amorphous halos. Graphite shells are observed in some MMG NPs that have a

high affinity for C, such as Fe (**a**), Co (**f**) and Ni (**n**), where it is possible that the C source comes from the degradation of ethanol^{37,38}. The spacing between the layer structures in **a**, **f** and **n** is about 3.6 Å, which matches with that of graphite. The fcc structures referred to in this figure include face-centred diamond cubic (Ge) and close-packed fcc metals. The preparation parameters for the monatomic metals are listed in Supplementary Table 2. Scale bars, 5 nm.

with a sufficient electron dose^{11,28}. The coalescence also indicates that the amorphous regions are pure Au. Similar transitions were observed on individual Au (Fig. 2b) and Ru MMG NPs (Fig. 2c). These glass-to-crystal transitions confirm that the single Au and Ru metals were vitrified by our method.

To demonstrate the universality of this method, we systematically studied the feasibility of vitrifying more monatomic metals, including metals with bcc, hcp and fcc crystal structures. Applying this method, we vitrified more than a dozen (a total of 17) monatomic metals into glassy states and obtained various MMG NPs (Fig. 3). Figure 3a–d shows the results for bcc metals iron (Fe), vanadium (V), Ta and tungsten (W), respectively, which can also be vitrified by other methods⁷¹. Figure 3e–h shows the MMG NPs vitrified from the hcp metals hafnium (Hf), cobalt (Co), zirconium (Zr) and Ru, respectively. Figure 3i–p shows more MMGs produced from fcc metals including both main group (aluminium (Al) and germanium (Ge)) and transition group metals (Pd, iridium (Ir), silver (Ag), Ni, copper (Cu) and platinum (Pt)). Whereas the HR-TEM images of all of the MMG NPs show amorphous structures, confirmed by the diffusive amorphous halos in the FFT images, we observed a C shell around some amorphous particles (marked in Fig. 3a,f,n), such as

Fe, Co and Ni, which all have a high affinity for C (ref. 24). However, no C shell was observed surrounding the other MMG NPs, as confirmed via EELS measurements for W (Supplementary Fig. 2) and chemical valence measurements via XPS for Ag (Supplementary Fig. 3). Similar results have been observed for other fcc metals including Pd, Ag and Pt. Several fully amorphous and partially amorphous NPs were obtained in one batch (Supplementary Figs. 4–6).

Previous studies have shown that as soon as crystal nucleation exists, monatomic metals have fast crystal growth rates from their melts^{29,30}. Therefore, the key issue of vitrifying monatomic metals lies in suppressing the crystal nucleation, especially the heterogeneous crystal nucleation caused by contaminants. Pulsed laser ablation in liquid is a complex process due to the intrinsic short timescales and several phenomena occurring simultaneously^{24–27}. When the target is ablated, a large number of NPs are produced, and some may enter the cavitation bubble where temperatures can reach 1,000–10,000 K. These NPs may remain separate or merge until the cavitation bubble collapses, and subsequently they are exposed to the liquid medium and undergo a rapid cooling process from a high temperature to room temperature. Concurrently, some other NPs may be directly ejected

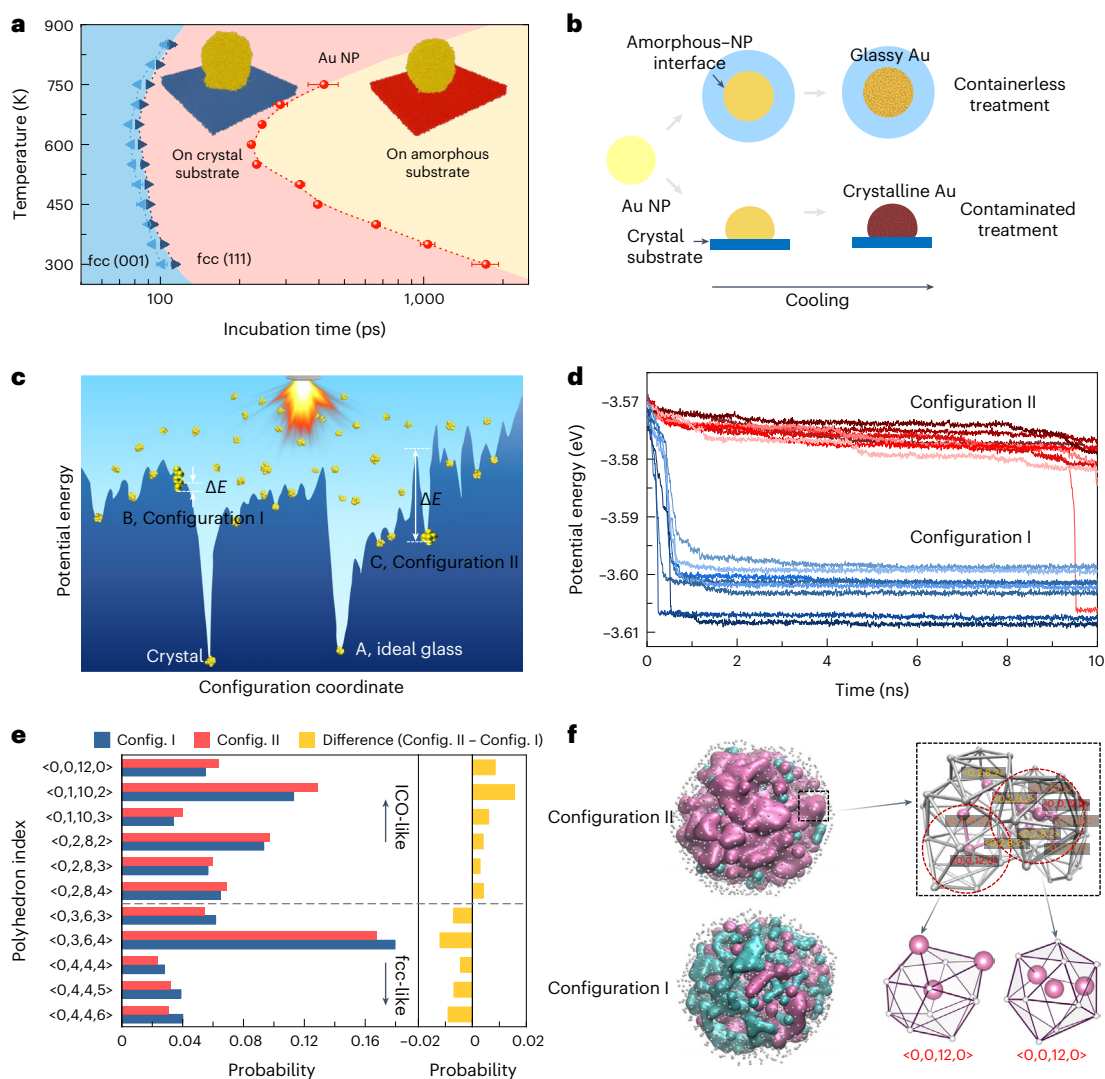


Fig. 4 | Effect of the liquid medium and the origin of stability disclosed via MD simulations. **a**, The TTT diagram of monatomic Au obtained from MD simulations. Au NPs with a diameter of 8 nm were located on an amorphous Au substrate and on Au fcc (001) and fcc (111) crystal substrates, respectively, for quenching. The amorphous substrate is analogous to the liquid medium and the crystal substrate acts as a heterogeneous nucleation precursor. The characteristic points for these three cases are calculated as the red, light blue and dark blue curves. The error bars represent the standard deviation of six independent measurements. **b**, Schematic of an Au NP quenched in the liquid medium (containerless/uncontaminated treatment; top) and on a crystal substrate (contaminated treatment; bottom) to form glassy Au and crystalline Au, respectively. **c**, Schematic of a PEL. Location A indicates the ideal glass; locations B and C indicate the unstable and stable glasses, corresponding to

the prepared unstable Au glassy NPs (Configuration I) and stable Au glassy NPs (Configuration II), respectively. The single yellow sphere in **c** represents a cluster. **d**, The crystallization processes of eight unstable (Configuration I) and eight stable (Configuration II) Au MMG NPs with the incubation time, extracted from 20 simulated Au MMG NPs (Supplementary Fig. 8). **e**, The probability of different coordination polyhedra (different Voronoi indices) in Configurations I and II. The polyhedra are shown in blue and red for Configurations I and II, respectively. The yellow columns show the probability differences between the configurations, where these data show more icosahedron-like (ICO-like) packings in Configuration II and more crystal-like (fcc-like) packings in Configuration I. **f**, Atomic structures of Configurations I and II, consisting of an ICO-like region (purple), an fcc-like ordered region (cyan) and liquid-like atoms (white).

into the liquid medium^{26,27} to undergo a similar rapid cooling process. On contact with the hot NPs, the surrounding ethanol absorbs and dissipates the heat of the NPs. During this process, the surrounding ethanol may evaporate, instantaneously forming a thin layer of ethanol gas. Subsequently, the heat and ethanol gas are absorbed by the outer liquid medium. This enables extremely high cooling rates during the cooling of the NPs. Meanwhile, the liquid medium creates a containerless/uncontaminated condition for cooling the NPs, which promotes the formation of amorphous structures by suppressing heterogeneous nucleation. Consequently, the liquid medium plays a pivotal role during the cooling process by providing ultrafast cooling rates and creating a containerless/uncontaminated condition, which in turn suppresses

heterogeneous nucleation and enables the formation of amorphous structures in the NPs.

To illustrate the effect of the liquid medium during the cooling stage, MD simulations were performed for the Au model system with two different kinds of substrate. One NP was located on an amorphous substrate, analogous to uncontaminated conditions in a liquid medium; the other was located on crystalline substrates (fcc (100) and fcc (111)) that provide heterogeneous nucleation (see the insets in Fig. 4a). We explored the time–temperature–transformation (TTT) diagram^{31,32} (Methods), which describes the critical cooling rate for glass formation and the occurrence of crystallization events as a function of the isothermal temperature and incubation time^{33,34}. As shown in Fig. 4a,

the TTT curves for the two crystalline substrates (light and dark blue dashed curves) show no marked difference, and the characteristic crystallization nose points (CCNPs) of the two blue curves are close. However, the CCNP is much lowered when the metallic NP is cooled on an amorphous substrate (red curve in Fig. 4a), indicating that the possibility of heterogeneous nucleation and growth of liquid Au is reduced markedly, along with a lower critical cooling rate on an uncontaminated cooled substrate (the corresponding maximum cooling rate at the CCNP is close to 10^{13} K s⁻¹). Previous experimental studies have shown that fcc metals cannot vitrify at a cooling rate as high as 10^{14} K s⁻¹ (ref. 7), but MD simulations have shown that it is possible to prepare Cu MMG at a cooling rate of 10^{12} – 10^{13} K s⁻¹ in an uncontaminated environment^{31,32}. Our experimental results demonstrate that the vitrification of fcc monatomic metals can be achieved at a very similar cooling rate (10^{13} K s⁻¹ (ref. 26)), indicating the important contributions of the liquid medium to the formation of the MMG, that is, an ultrafast cooling rate, suppressing heterogeneous nucleation and promoting glass formation. We prepared a schematic diagram to compare the containerless/uncontaminated condition with the contaminated treated boundary condition during the rapid cooling of Au NPs (Fig. 4b). Our simulations agree with our experimental observation that noble fcc metals, including Au, can be vitrified under the containerless/uncontaminated condition during the rapid cooling process. In addition, reducing the sample size to generate nanoscale particles via this method can reduce the likelihood of encountering contaminants in these small volumes, thereby reducing the likelihood of heterogeneous nucleation, which promotes the formation of amorphous structures^{35,36}.

Using our method, numerous NPs with diverse atomic configurations and distributed energies can be obtained simultaneously during the preparation of one batch. During the process of image acquisition for the Au MMGs, we found that the Au MMG NPs crystallized at different rates under electron-beam irradiation (Supplementary Fig. 7), indicating they have different stabilities. Extensive studies on rejuvenation and ultrastable glass have suggested that, by modulating the topological frustration of the configurations, the stability of the glass can be changed notably^{37,38}. The glass stability is intrinsically governed by the configuration. A key problem is to discover the structural basis that controls the stability of the configuration. Thus, MD simulations were performed to explore the effect of the atomic configuration on glass stability (Methods). One hundred Au MMG NPs were independently superquenched to 300 K, providing a library of 100 glass configurations, which is analogous to the experimental results. Each configuration was relaxed at 300 K for 10 ns, and then its resistance to crystallization was analysed. The crystallization incubation times of these configurations are quite different and show diverse glass stabilities (Supplementary Fig. 8). To better understand this issue, we propose that MMG NPs with different stabilities are located in different basins of the PEL (Fig. 4c), which shows the configurational dependence of the glass stability. These kinds of stable amorphous configuration may be located in the locally deep basins in the PEL (such as locations A and C in Fig. 4c)²¹. According to the crystallization time of the 100 configurations, the most and least stable configurations were determined and their differences in atomic structure were analysed. As shown in Fig. 4d, unstable configurations (such as Configuration I) crystallized within 0.1 ns, whereas stable configurations (such as Configuration II) remained amorphous all of the time. Configurations I and II are located in two different basins in the PEL (Fig. 4c). When relaxed at the same temperature, Configuration I can easily fall into the deep basin of the crystal when it has passed the small energy barrier, whereas Configuration II can be stabilized in the metastable basin. Configuration II shows a higher ability to resist devitrification than Configuration I, demonstrating that there can be some specific atomic packing in Configuration II to promote the stability, which is related to the distribution of coordination polyhedra in MGs^{37,39}. As shown in Fig. 4e, the atomic cluster distributions show some differences between the stable and

unstable configurations. The stable Au glass configurations have more icosahedra-like clusters, such as $\langle 0,0,12,0 \rangle$, $\langle 0,1,10,2 \rangle$ and $\langle 0,2,8,2 \rangle$, which contain a higher proportion of faces with five-fold symmetry, whereas unstable Au glass configurations have more crystal-like clusters, such as $\langle 0,4,4,4 \rangle$, $\langle 0,4,4,5 \rangle$ and $\langle 0,4,4,6 \rangle$, which contain a lower proportion faces with five-fold symmetry but a higher proportion faces with four/six-fold symmetry. The atomic structures of the two glasses are shown in Fig. 4f, from which the icosahedra-like clusters are shown.

According to Kauzmann's hypothesis¹, the glass transition is intrinsically caused by topological frustration, which inhibits both the relaxation dynamics and crystallization. It predicts that, if crystallization is avoided, the configurations with stronger topological frustration can stabilize the glass and finally lead to the most stable glass, that is, the ideal glass. The ideal glass (at location A in Fig. 4c) can be ultrastable with both high thermal and kinetic stabilities. However, mostly, the stability of the glass is determined by the relative energy barrier. The glass in a locally deep basin, such as at location C, can be stable due to the large kinetic activation energy ΔE . These kinds of configuration exist widely in MGs. Frank attributed the stability to this topological frustration as the formation of local icosahedral clusters⁴⁰. In the decades since then, abundant studies have observed that icosahedral-like clusters, which exist in metallic supercooled liquids⁴¹ and glasses⁴², work as a strong suppression of both relaxation dynamics and crystallization^{43,44}. Therefore, it is reasonable to conclude that in Configuration I, the fewer icosahedra-like clusters generate weak topological frustration and the more crystal-like clusters act as promoters of crystallization; by contrast, in Configuration II, more icosahedral-like clusters causes topological frustration to beat the ordering transition, achieving better stability of the amorphous state. The production of a large number of configurations provides more opportunities for obtaining stable configurations that more icosahedral-like clusters. It shows a strategy for enhancing crystallization resistance by adding icosahedral-like structures to the glass configurations.

To explore the effect of liquid ethanol during the vitrification process further, Au was ablated via pulsed laser ablation under vacuum conditions and a protective argon (Ar) atmosphere (Supplementary Fig. 9). The samples under vacuum/Ar conditions display crystalline chain-like structures, making the formation of amorphous structures difficult. The strong surface tension and hydrostatic pressure interaction between metal NPs and liquid ethanol is a key factor, which acts as a strong constraint on the NPs, enhances atomic cohesion, promotes solidification and helps to stabilize the amorphous structure. Thus, in a uniformly cooled liquid ethanol environment, regular spherical NPs are generated. By contrast, under vacuum/protective-gas conditions, the surface tension is weak, the diffusion is fast, the shape is irregular and the cooling is not uniform, which is not conducive to the formation of a glass.

In summary, we present the vitrification of fcc Au into the glassy state, which also occurs for other fcc, hcp and bcc monatomic metals. The formation of the Au MMG is attributed to rapid cooling and the suppression of heterogeneous nucleation. Rapid cooling can be achieved during the process of ultrafast pulsed laser ablation in liquid, where the appropriate liquid medium is vital to the vitrification of noble fcc metals. The two benefits provide an ideal environment for amorphization and considerably suppress the heterogeneous nucleation and growth of crystals. This strategy can produce a library of atomic configurations for obtaining MMGs with different stabilities, some of which may be extremely stable.

Online content

Any methods, additional references, Nature Portfolio reporting summaries, source data, extended data, supplementary information, acknowledgements, peer review information; details of author contributions and competing interests; and statements of data and code availability are available at <https://doi.org/10.1038/s41563-024-01967-0>.

References

1. Kauzmann, W. The nature of the glassy state and the behavior of liquids at low temperatures. *Chem. Rev.* **43**, 219–256 (1948).
2. Turnbull, D. Kinetics of solidification of supercooled liquid mercury droplets. *J. Chem. Phys.* **20**, 411–424 (1952).
3. Turnbull, D. & Cohen, M. H. Concerning reconstructive transformation and formation of glass. *J. Chem. Phys.* **29**, 1049–1054 (1958).
4. Turnbull, D. Under what conditions can a glass be formed? *Contemp. Phys.* **10**, 473–488 (1969).
5. Cohen, M. H. & Turnbull, D. Metastability of amorphous structures. *Nature* **203**, 964 (1964).
6. Bhat, M. H. et al. Vitrification of a monatomic metallic liquid. *Nature* **448**, 787–790 (2007).
7. Zhong, L., Wang, J., Sheng, H., Zhang, Z. & Mao, S. X. Formation of monatomic metallic glasses through ultrafast liquid quenching. *Nature* **512**, 177–180 (2014).
8. Greer, A. L. New horizons for glass formation and stability. *Nat. Mater.* **14**, 542–546 (2015).
9. Davies, H. A., Aucote, J. & Hull, J. B. Amorphous nickel produced by splat quenching. *Nat. Phys. Sci.* **246**, 13–14 (1973).
10. Nestell, J. E., Scoles, K. J. & Christy, R. W. Optical conductivity of amorphous Ta and β -Ta films. *J. Appl. Phys.* **53**, 8993–8998 (1982).
11. Kim, Y. W., Lin, H. M. & Kelly, T. F. Amorphous solidification of pure metals in submicron spheres. *Acta Metall.* **37**, 247–255 (1989).
12. Suslick, K. S., Choe, S.-B., Cichowlas, A. A. & Grinstaff, M. W. Sonochemical synthesis of amorphous iron. *Nature* **353**, 414–416 (1991).
13. Zhao, R. et al. A facile strategy to produce monatomic tantalum metallic glass. *Appl. Phys. Lett.* **117**, 131903 (2020).
14. Lee, M. C., Kendall, J. M. & Johnson, W. L. Spheres of the metallic glass $\text{Au}_{55}\text{Pb}_{22.5}\text{Sb}_{22.5}$ and their surface characteristics. *Appl. Phys. Lett.* **40**, 382–384 (1982).
15. Herlach, D. M., Cochrane, R. F., Egry, I., Fecht, H. J. & Greer, A. L. Containerless processing in the study of metallic melts and their solidification. *Int. Mater. Rev.* **38**, 273–347 (1993).
16. Kui, H., Greer, A. L. & Turnbull, D. Formation of bulk metallic glass by fluxing. *Appl. Phys. Lett.* **45**, 615–616 (1984).
17. Nishiyama, N. et al. The world's biggest glassy alloy ever made. *Intermetallics* **30**, 19–24 (2012).
18. Castellero, A. et al. Improvement of the glass-forming ability of $\text{Zr}_{55}\text{Cu}_{30}\text{Al}_{10}\text{Ni}_5$ and $\text{Cu}_{47}\text{Ti}_{34}\text{Zr}_{11}\text{Ni}_8$ alloys by electro-deoxidation of the melts. *Scr. Mater.* **55**, 87–90 (2006).
19. Yang, B. J., Lu, W. Y., Zhang, J. L., Wang, J. Q. & Ma, E. Melt fluxing to elevate the forming ability of Al-based bulk metallic glasses. *Sci. Rep.* **7**, 11053 (2017).
20. Lin, X. H., Johnson, W. L. & Rhim, W. K. Effect of oxygen impurity on crystallization of an undercooled bulk glass forming Zr–Ti–Cu–Ni–Al alloy. *Mater. Trans. JIM* **38**, 473–477 (1997).
21. Debenedetti, P. G. & Stillinger, F. H. Supercooled liquids and the glass transition. *Nature* **410**, 259–267 (2001).
22. Liu, Y. H., Fujita, T., Aji, D. P., Matsuura, M. & Chen, M. W. Structural origins of Johari–Goldstein relaxation in a metallic glass. *Nat. Commun.* **5**, 3238 (2014).
23. Nagata, S., Ogino, M. & Taniguchi, S. Electrical resistivity of thin metal films vapor-quenched at 77 K. Cu, Ag, Au, Ni, Pd, and Pt. *Phys. Status Solidi A* **102**, 711–717 (1987).
24. Amendola, V. & Meneghetti, M. What controls the composition and the structure of nanomaterials generated by laser ablation in liquid solution? *Phys. Chem. Chem. Phys.* **15**, 3027–3046 (2013).
25. Liang, S. X., Zhang, L. C., Reichenberger, S. & Barcikowski, S. Design and perspective of amorphous metal nanoparticles from laser synthesis and processing. *Phys. Chem. Chem. Phys.* **23**, 11121–11154 (2021).
26. Shih, C. Y. et al. Two mechanisms of nanoparticle generation in picosecond laser ablation in liquids: the origin of the bimodal size distribution. *Nanoscale* **10**, 6900–6910 (2018).
27. Shih, C.-Y. et al. Limited elemental mixing in nanoparticles generated by ultrashort pulse laser ablation of AgCu bilayer thin films in a liquid environment: atomistic modeling and experiments. *J. Phys. Chem. C* **125**, 2132–2155 (2021).
28. Jeon, S. et al. Reversible disorder–order transitions in atomic crystal nucleation. *Science* **371**, 498–503 (2021).
29. Ashkenazy, Y. & Averback, R. S. Kinetic stages in the crystallization of deeply undercooled body-centered-cubic and face-centered-cubic metals. *Acta Mater.* **58**, 524–530 (2010).
30. Tang, C. & Harrowell, P. Anomalously slow crystal growth of the glass-forming alloy CuZr. *Nat. Mater.* **12**, 507–511 (2013).
31. An, Q. et al. Synthesis of single-component metallic glasses by thermal spray of nanodroplets on amorphous substrates. *Appl. Phys. Lett.* **100**, 041909 (2012).
32. An, S. et al. Ultrasmall nanoparticles inducing order-to-disorder transition. *Phys. Rev. B* **98**, 134101 (2018).
33. Johnson, W. L. Bulk glass-forming metallic alloys: science and technology. *MRS Bull.* **24**, 42–56 (1999).
34. Schroers, J., Wu, Y., Busch, R. & Johnson, W. L. Transition from nucleation controlled to growth controlled crystallization in $\text{Pd}_{43}\text{Ni}_{10}\text{Cu}_{27}\text{P}_{20}$ melts. *Acta Mater.* **49**, 2773–2781 (2001).
35. Turnbull, D. & Cech, R. E. Microscopic observation of the solidification of small metal droplets. *J. Appl. Phys.* **21**, 804–810 (1950).
36. Turnbull, D. Formation of crystal nuclei in liquid metals. *J. Appl. Phys.* **21**, 1022–1028 (1950).
37. Singh, S., Ediger, M. D. & de Pablo, J. J. Ultrastable glasses from in silico vapour deposition. *Nat. Mater.* **12**, 139–144 (2013).
38. Sun, Y., Concustell, A. & Greer, A. L. Thermomechanical processing of metallic glasses: extending the range of the glassy state. *Nat. Rev. Mater.* **1**, 16039 (2016).
39. Sheng, H. W., Ma, E. & Kramer, M. J. Relating dynamic properties to atomic structure in metallic glasses. *JOM* **64**, 856–881 (2012).
40. Frank, F. C. Supercooling of liquids. *Proc. R. Soc. A* **215**, 43–46 (1952).
41. Lee, G. W. et al. Difference in icosahedral short-range order in early and late transition metal liquids. *Phys. Rev. Lett.* **93**, 037802 (2004).
42. Hirata, A. et al. Geometric frustration of icosahedron in metallic glasses. *Science* **341**, 376–379 (2013).
43. Shen, Y. T., Kim, T. H., Gangopadhyay, A. K. & Kelton, K. F. Icosahedral order, frustration, and the glass transition: evidence from time-dependent nucleation and supercooled liquid structure studies. *Phys. Rev. Lett.* **102**, 057801 (2009).
44. Kelton, K. F. et al. First X-ray scattering studies on electrostatically levitated metallic liquids: demonstrated influence of local icosahedral order on the nucleation barrier. *Phys. Rev. Lett.* **90**, 195504 (2003).

Publisher's note Springer Nature remains neutral with regard to jurisdictional claims in published maps and institutional affiliations.

Springer Nature or its licensor (e.g. a society or other partner) holds exclusive rights to this article under a publishing agreement with the author(s) or other rightsholder(s); author self-archiving of the accepted manuscript version of this article is solely governed by the terms of such publishing agreement and applicable law.

© The Author(s), under exclusive licence to Springer Nature Limited 2024

Methods

Specimen preparation

The purity of all of the studied metals (ZhongNuo Advanced Material) is listed in Supplementary Table 1. An all-solid-state ultraviolet laser with a wavelength of 355 nm, a pulse width of 7 ps, a maximum pulse energy of 20 μJ , a repetition frequency of 100 kHz to 2 MHz and a spot diameter of 20 μm was used. Before the experiments, the raw materials were cleaned via ultrasonication in ethanol. The bulk metallic target was placed in a clean beaker that had been washed first using acetone (99.5%) and then with ethanol (99.9%). The metal target was submerged in the liquid to a depth of 1–2 mm. To minimize the dissolved O in ethanol, nitrogen gas was bubbled through the ethanol for 60 min (flow rate, 4 litres per min). The laser beam was accurately focused on to the surface of the target vertically through the liquid medium in a closed chamber. After laser ablation for 1 min, the fresh monatomic NPs were dispersed via sonication and centrifuged for collection in the ethanol solution. The influence of the parameters on the frequency of the amorphous NPs for different metals was studied, and the results are shown in Supplementary Fig. 10.

Specimen characterization

The resulting NPs were dispersed in ethanol and deposited on to Si_3N_4 membrane substrates. The morphology and microstructure of the NPs were observed via HR-TEM (using Titan G2 60-300 and JEM-F200 electron microscopes), and images of the disordered structures at atomic resolution were acquired using double spherical aberration-corrected TEM (using JEM-ARM300F, FEI Titan³ Themis G2 300 and Thermo Fisher Spectra 300 instruments). The high-angle annular dark-field scanning transmission electron microscopy images were obtained at 300 kV.

The in situ irradiation of the MMGs with a high accelerating voltage in TEM was conducted for the amorphous samples to observe the disorder-to-order transition. The ordering process of the MMGs was recorded using a camera with a temporal resolution of 0.04 s with the JEM-ARM300F instrument (Fig. 2a and Supplementary Video 1), the Thermo Fisher Spectra 300 microscope (Fig. 2b and Supplementary Figs. 4–6 and 9), the FEI Titan³ Themis G2 300 instrument (Fig. 2c) and the JEM-F200 electron microscope (Supplementary Fig. 7).

Assessing the amorphous structure and monometallic composition

Because MMGs made from fcc metals such as Au, Ag, Pd, Pt and Ir undergo rapid disordered to ordered transformation under electron irradiation, it is necessary to complete the capture of amorphous structures as soon as possible. The TEM observations were conducted according to the following steps:

1. Using a resolution of $4,096 \times 4,096$ pixels, an area with a dispersed distribution of numerous NPs was sought. The beam was focused on to the NPs to adjust the imaging parameters that included the voltage, current, focus, magnetization and beam convergence, to avoid conditions such as off-axis aberrations. The electron dose rate was about $1,000\text{--}1,500 \text{ e} \text{ \AA}^{-2} \text{ s}^{-1}$.
2. When capturing the atomic structure, a live FFT image was simultaneously created to observe the diffraction patterns.
3. The focused area was shifted slightly to capture the amorphous morphology of the NPs so that it would not take a long time to calibrate the beam and would minimize any notable irradiation effects on the atomic structure from the ultrahigh voltage electrons. The electron dose rate for capturing the images was enhanced to about $1,500\text{--}3,000 \text{ e} \text{ \AA}^{-2} \text{ s}^{-1}$.
4. After capturing one image, the shutter was immediately closed to block the electron beam and reduce the damaging effects of the beam.

Verification of the monometallic composition was carried out via EELS measurements using the FEI Titan³ Themis G2 300 and Thermo

Fisher Spectra 300 instruments with a GIF Continuum K3 (Model 1069) detector (Supplementary Notes).

XPS measurements were carried out using a Thermo Fisher ESCALAB XI⁺ probe to examine the chemical compositions and valence states. The XPS measurements were conducted according to the procedures as described in the Supplementary Notes.

Modelling of the MD simulations

Using the large-scale atomic/molecular massively parallel simulator (or LAMMPS)⁴⁵, we carried out MD simulations to investigate the benefit(s) of the uncontaminated conditions on the MMG formation. During the simulations, the many-body embedded-atom method (or EAM)⁴⁶ potential was used to describe the interactions between the Au atoms, and the time step was set to 2 fs.

To show the uncontaminated covering effect on the metallic NPs in the liquid medium, we used a particle–substrate model. A similar simulation was conducted in a previous study³¹. Three different substrates were provided—one amorphous Au substrate and two crystalline Au substrates—to simulate the effect of contact between the metallic liquid and either uncontaminated conditions or heterogeneous nucleant precursors during cooling. The substrate system was composed of 50,000 atoms, and the sample size was around $20 \times 20 \times 2 \text{ nm}$. To consider different orientations, the crystalline Au substrates were generated along the (001) and (111) directions of the fcc lattice, respectively. The crystalline structures were then relaxed at 300 K for 1 ns. The amorphous substrate was obtained through fast quenching from the liquid to the amorphous state. At first, the amorphous substrate was heated to 2,000 K for 10 ns, which is much higher than the melting temperature, and then it was quenched to 300 K at a rate of 10^{14} K s^{-1} . During the substrate generation process, periodic boundary conditions were used with an isothermal–isobaric (*NPT*) ensemble; the temperature was controlled using a Nosé–Hoover thermostat⁴⁷, and the pressure was maintained at 0 bar using a Parrinello–Rahman barostat⁴⁸. The NP, which contained 27,000 atoms with a diameter of 8 nm, was maintained at 2,000 K using a canonical sampling thermostat⁴⁹ for 10 ns with free boundary conditions. The NP was then placed at the centre of the substrate and relaxed for 0.5 ns with fixed boundary conditions, that is, the substrate was pinned, and only the NP was relaxed through the canonical sampling thermostat. The system size was $20 \times 20 \times 14 \text{ nm}$.

TTT curves

To obtain the TTT curve of the NP on the substrate, the NP was directly maintained at the target temperature, and the incubation time τ_x of the target temperature was recorded when the degree of crystallization reached the criterion. The degree of crystallization was measured using the parameter F_6 (ref. 50), which is defined as

$$F_6 = \frac{1}{N} \sum_{i=1}^N f_6(i), \quad (1)$$

where N is the number of atoms in the NP, and $f_6(i)$ is the atomic level crystallization parameter. The latter can be determined by the standard bond-order parameter $q_{6m}(i)$ (ref. 51) and the neighbourhood environment (S_6)⁵² as

$$f_6 = \frac{1}{N_c(i)} \sum_{j \in N_c(i)} \Theta(S_6(i,j) - 0.7), \quad (2)$$

$$S_6(i,j) = \frac{\sum_{m=-6}^6 q_{6m}(i) \cdot q_{6m}^*(j)}{\left| \sum_{m=-6}^6 q_{6m}(i) \right| \left| \sum_{m=-6}^6 q_{6m}(j) \right|}, \quad (3)$$

where $\Theta(x)$ is the step function, $N_c(i)$ is the nearest neighbour of atom i , and m is an integer from -6 to 6 . q_{6m}^* is the complex conjugate of q_{6m} . The time at which the F_6 of the system reached 0.5 was considered

to be the incubation time τ_x . The TTT curves were then obtained, as shown in Fig. 4a.

Configuration dependence of stability in MD simulations

One hundred Au MMG NPs were generated independently, providing a library of glass configurations with different stabilities. Each sample was first melted and equilibrated at 2,000 K for 0.1 ns, and then quenched to 300 K at a cooling rate of 10^{14} K s⁻¹. Finally, each sample was relaxed at 300 K for 10 ns to investigate its stability against crystallization. For comparison, the Au NP studied here has a diameter of around 4 nm (and contains 1,853 Au atoms), close to the experimental measurements. As shown in Supplementary Fig. 8, the potential energy drops (crystallization) for different configurations occur at different moments, indicating their different stabilities. Whereas crystallization of most of the configurations occurs between 1 and 5 ns, some unstable configurations crystallize within 0.5 ns. There are some stable configurations that do not even crystallize during the whole simulation process of 10 ns. We selected the most unstable and stable configurations (Fig. 4d), named as Configurations I and II, respectively, to study their structural differences. The Voronoi index values of two MMGNPs (Configuration I and Configuration II) with different probabilities are shown in Fig. 4e. The results suggest that preparing a large number of glass samples simultaneously contributes to generating stable configurations, which contain more icosahedral-like clusters that enhance the glass stability against crystallization for the MMG.

Data availability

All data that support the findings of this study are available within the article and its Supplementary Information.

References

45. Plimpton, S. Fast parallel algorithms for short-range molecular dynamics. *J. Comput. Phys.* **117**, 1–19 (1995).
46. Olsson, P. A. Transverse resonant properties of strained gold nanowires. *J. Appl. Phys.* **108**, 034318 (2010).
47. Hoover, W. G. Canonical dynamics: equilibrium phase-space distributions. *Phys. Rev. A* **31**, 1695–1697 (1985).
48. Parrinello, M. & Rahman, A. Polymorphic transitions in single crystals: a new molecular dynamics method. *J. Appl. Phys.* **52**, 7182–7190 (1981).
49. Bussi, G., Donadio, D. & Parrinello, M. Canonical sampling through velocity rescaling. *J. Chem. Phys.* **126**, 014101 (2007).
50. Goodrich, C. P., Liu, A. J. & Nagel, S. R. Solids between the mechanical extremes of order and disorder. *Nat. Phys.* **10**, 578–581 (2014).
51. Auer, S. & Frenkel, D. Numerical prediction of absolute crystallization rates in hard-sphere colloids. *J. Chem. Phys.* **120**, 3015–3029 (2004).

52. Steinhardt, P. J., Nelson, D. R. & Ronchetti, M. Bond-orientational order in liquids and glasses. *Phys. Rev. B* **28**, 784–805 (1983).

Acknowledgements

This work was supported by Guangdong Major Project of Basic and Applied Basic Research, China (grant number 2019B030302010 (H.-Y.B.)), the National Natural Science Foundation of China (grant numbers 52192601 (H.-Y.B.), 52192602 (H.-Y.B.), 52071222 (H.-B.K.), 61888102 (W.-H.W.), 11790291 (W.-H.W.), 22172003 (J.Z.), 52001219 (X.T.), 52301214 (H.-P.Z.) and 52130108 (B.-S.S.)) and the Strategic Priority Research Program of the Chinese Academy of Sciences (XDB30000000 (W.-H.W.)). We acknowledge the computational resource provided by the Platform for Data-Driven Computational Materials Discovery of Songshan Lake Materials Laboratory. We acknowledge M.-J. Zou and X.-L. Ma of the Bay Area Centre for Electron Microscopy at Songshan Lake Materials Laboratory for the use of the double spherical aberration-corrected Thermo Fisher Spectra 300 instrument, and the Electron Microscopy Laboratory at Peking University for the use of aberration-corrected Titan³ Themis G2 200 instrument.

Author contributions

H.-Y.B. and W.-H.W. supervised the work. X.T., W.-H.W., J.Z. and H.-Y.B. designed the experiments. Y.-E.Z. and X.T. operated the laser ablation. X.T., Y.-E.Z., G.W., Z.L., Y. Zhang and J.Z. carried out the electron microscopy experiments. Y.-E.Z. performed the XPS tests. B.-S.S., H.-P.Z., Z.L., J.Z., H.-Y.B. and W.-H.W. performed the modelling and simulations. H.-Y.B., X.T., H.-P.Z., B.-S.S. and J.Z. wrote the manuscript. H.-Y.B. and X.T. responded to the reviewers' comments. B.Z., Y.-H.L., Y. Zhao and H.-B.K. participated in discussions. All of the authors contributed to the analysis and interpretation of the data.

Competing interests

The authors declare no competing interests.

Additional information

Supplementary information The online version contains supplementary material available at <https://doi.org/10.1038/s41563-024-01967-0>.

Correspondence and requests for materials should be addressed to Hai-Bo Ke, Jihan Zhou or Hai-Yang Bai.

Peer review information *Nature Materials* thanks Howard Sheng and the other, anonymous, reviewer(s) for their contribution to the peer review of this work.

Reprints and permissions information is available at www.nature.com/reprints.